# Laterally Modulating Carrier Concentration by Ion Irradiation in CdO Thin Films for Mid-IR Plasmonics

Angela J. Cleri[1], Mingze He[2,3], Maxwell J. Tolchin[1], Christopher Gubbin[4,5], Eric Lang,[6,7] Khalid Hattar[7,8], Simone De Liberato[4,5,9], Joshua D. Caldwell[2,5], and Jon-Paul Maria[1]

[1] Department of Materials Science and Engineering, The Pennsylvania State University, University Park, PA, USA
[2] Mechanical Engineering, Vanderbilt University, Nashville TN, USA
[3] Photonics Initiative, Advanced Science Research Center, City University of New York, New York, NY 10031, USA
[4] School of Physics and Astronomy, University of Southampton, Southampton, SO17 1BJ, UK
[5] Sensorium Technological Laboratories, Nashville, TN, USA
[6] Department of Nuclear Engineering, University of New Mexico, Albuquerque, NM, USA
[7] Center for Integrated Nanotechnology, Sandia National Laboratory, Albuquerque, NM, USA
[8] Department of Nuclear Engineering, University of Tennessee, Knoxville, TN USA
[9] Istituto di Fotonica e Nanotecnologie – Consiglio Nazionale delle Ricerche (CNR), Milano, Italy

## Abstract

This report demonstrates tunable carrier densities in CdO thin films through local ion irradiation, providing lateral control of mid-IR optical properties. Ion-solid interactions produce donor-like defects that boost electron concentrations from the practical minimum in unintentionally-doped material of $2.5\times10^{19}$ $cm^{-3}$ to a maximum of $2.5\times10^{20}$ $cm^{-3}$ by metered ion exposure. This range is achieved using He, N, Ar, or Au ions at 1-2.8 MeV; when normalized by displacement damage dose, all ion species produce comparable results. Since CdO is well-described by the Drude model, irradiation-tuned carrier densities directly alter the infrared dielectric function, and in turn, mid-infrared optical properties. We further demonstrate that by combining irradiation with traditional lithography, CdO films exposed to ions in the presence of 3-μm thick, patterned ion-blocking photoresist exhibit lateral carrier density profiles with approximately 400-nm resolution. Scanning near-field optical microscopy reveals sharp optical interfaces with almost no companion contrast in surface morphology, microstructure, or crystallinity. Finally, we demonstrate CdO lateral homostructures supporting surface plasmon polaritons (SPPs) whose dispersion relation can be tuned through periodic patterning in a monolithic platform by simple nanofabrication. Numerical simulations show these polaritons result from strong coupling between excitations at CdO plasma frequencies, and SPPs supported by the platinum substrate.

## Introduction

Confining light to deeply sub-diffractional length scales is a principal goal for nanophotonics research. This is achieved frequently by engineered interfaces separating materials with different dielectric and/or optical properties that bind light waves to coherent carrier oscillations in a conducting medium. Engineering such interfaces in semiconducting thin films is conveniently accomplished in stacked heterostructures by tailoring the carrier concentration of individual layers which, in turn, tunes their dielectric functions such that, at a frequency of interest, the desired permittivity contrast, i.e., metallic vs. transparent, is present. Transparent conducting oxides (TCOs) are interesting in this context because their carrier concentrations can be controlled by doping[1–4] with a dynamic range that supports plasma frequencies spanning much of the infrared spectrum, and in particular, the mid-wave energy band, while remaining transparent in the visible spectral range.[5]

Cadmium oxide (CdO) is a TCO with exceptional plasmonic properties in the near to long-wave infrared (MIR) spectral range . Extrinsic donor doping supports carrier concentration ($n$) between $10^{19}$-$10^{21}$ $cm^{-3}$ while maintaining mobilities between 300-500 $cm^2/V{\cdot}s$, with the low effective electron mass at such high carrier concentrations providing a distinguishing material feature. These transport properties enable low-loss plasmonic modes within the ~2-9 μm free-space wavelength range.[4,6–9] For example, dispersive surface plasmon polariton (SPP) modes and non-dispersive epsilon-near-zero (ENZ) modes are supported in CdO films and spectrally tuned by controlling carrier density and/or thickness.[4,6,8] ENZ modes are supported in CdO layers at energies near the CdO plasma frequency, where the real part of the permittivity crosses zero, within films where the layer thickness is at or smaller than λ/50, and two interface modes couple symmetrically,[10,11] with λ representing the free-space wavelength. Further, layering CdO films with different thicknesses and doping levels gives rise to more complex nanophotonic phenomena such as hyperbolic light dispersion,[12] multiple, independent epsilon-near-zero (ENZ) resonant modes supported within a single structure,[13] and strong coupling between ENZ and SPP modes.[14] In all cases, the plasmonic host is a CdO heterostructure stack with interfacial contrast that is solely dictated by the local carrier density. Such stacks are easily prepared in one deposition where the donor dopant flux is modulated with time during growth.

While finite accumulation and depletion will occur in $n|n^+$ CdO homojunctions, at the wavelengths and carrier densities of interest, the layers are well-approximated as homogeneous.[9,12] As discussed above, CdO stacks allow polaritonic dispersion engineering that supports multiple individual and coupled modes by interfacial dielectric function contrast in the out-of-plane direction. Accessing comparable capabilities along the in-plane directions would grant two additional degrees of freedom, specifically, spatial and spectral coherence, with the former demonstrated by Greffet *et al.* for thermal emission, while the latter by multiple groups.[15–18] In most cases, this is accomplished by patterned combinations of dielectric and metallic materials, with the latter component introducing considerable losses, especially at IR energies.[19–21] In the present manuscript, we explore ion irradiation methods to laterally control carrier density, and thus the effective infrared dielectric function, enabling in-plane lateral homostructure designs for coherence control, waveguiding[22] and beam-steering[23] possibilities. Most importantly, these methods do not create microstructural boundaries between dissimilar materials with defects that scatter IR photons and interfere with high fidelity plasmon modes.

Recent reports explore metasurfaces with locally engineered optical properties through lateral doping using methods like dopant drive-in diffusion from spin-coated and patterned source layers,[24] and dopant implantation, *e.g.* phosphorous ions in silicon.[25] In addition, focused ion beam (FIB) has been used to implant gallium ions in zinc oxide to locally control carrier density and in vanadium dioxide to locally modify the metal-to-insulator transition temperature.[26] These methods all allow post-growth, lateral property control with minimal microstructure or physical interface creation. However, when laterally doping by ion implantation or drive-in, the profile depth and width can be difficult to control with arbitrary accuracy and may limit boundary sharpness or areal homogeneity. In addition, while the FIB technique can achieve very fine feature size resolution, there are practical considerations for large- area patterning. Further, these techniques introduce an extrinsic dopant ion that must be activated in the host, adding complexity to the fabrication process.

An alternative approach presented here uses higher energy ion beam irradiation. Here, the ions penetrate through the film coming to rest deep into the substrate; implanted species are not incorporated into the lattice and only defect cascades remain throughout the film thickness. In CdO, these defects, which likely introduce oxygen vacancies based on prior ion irradiation

experiments on CdO and similar materials,[27–30] act as donors and are compensated by electron charge carriers. This method has been used to generate damage in CdO thin films thereby increasing carrier concentration to explore Fermi level pinning in the material.[29,30] While ion implantation for doping thin films generally requires ion beam energies on the order of 10 keV, this type of ion irradiation occurs on the order of 1 MeV. This technique results in uniform transport properties throughout the film thickness and eliminates the dopant activation stage as well as the need to select ions that act as dopants in the host material in the first place, easing fabrication flexibility.

The combination of donor doping during deposition and inducing native donor defects through ion irradiation allows light manipulation at scales well below the free-space wavelength in all three dimensions in a single material system. Here, we investigate a suite of ion species and their effects on CdO transport, optical, crystalline, and morphological properties when irradiated at MeV energies. We further demonstrate local control of the CdO dielectric function by patterning gratings with varying periodicity between 6-12 μm (e.g., 6 μm periodicity corresponds to 3 μm ridges and 3 μm spacings) over a 5×5 mm area by ion irradiation through a photoresist mask. Sharp optical interfaces are confirmed through near-field optical measurements. In addition, far-field optical measurements are used to observe SPP modes propagating along gratings of both irradiated and non-irradiated regions. This optical response is corroborated by finite element method (FEM) simulations. Analytical calculations of the trilayer fully-coupled zone-folded dispersion relations in each grating region further demonstrate strong coupling behavior between CdO SPP modes and underlying Pt layers intended to mitigate evanescent field decay from the polariton modes. The combination of numerical simulations from FEM and analytical calculations of the underlying modal dispersions helps to streamline the design-to-fabrication process of irradiation patterned CdO lateral homostructures.

**Results**

To explore the effects of ion irradiation on CdO properties, square centimeter samples of as-deposited CdO thin films were treated by irradiation with several different ion species: 1 MeV helium ($He^+$), 1 MeV nitrogen ($N^+$), 1 MeV argon ($Ar^+$), and 2.8 MeV gold ($Au^{2+}$). For all ions, as the fluence (ions/$cm^2$) was increased the carrier density rose to a maximum value of about $2.3\times10^{20}$ $cm^{-3}$ as shown in Figure 1 a. SRIM calculations showed that for all cases, ions passed

through the CdO film and implanted deep in the substrate, leaving only a small ion concentration implanted into the film (see Supplemental Material). Thus, donor defects created by ion irradiation are native (point defects, i.e., oxygen vacancy – interstitial pairs, or incompletely displaced and ionized atoms), which are compensated by electron charge carriers. These defects also act as scattering sites, which reduce electron mobility, as shown in the bottom panel of Figure 1 a. Note that even prior to irradiation, as-deposited CdO films are considered "unintentionally doped" (UID) due to their intrinsically high oxygen vacancy concentrations, yielding a baseline carrier density of about $3\times10^{19}$ $cm^{-3}$.[6] Defects created by ion irradiation are not stable at elevated temperatures as shown in the Supplemental Material Figure S3, where carrier density decreases and mobility increases upon annealing.

While fluence accounts for the number of ions that reach the material over a given area, several other more standardized units have been developed by the irradiation-materials research community. In addition to fluence, transport property measurements are presented here as a function displacements per atom (dpa), a standard relationship for primary radiation damage production.[33] Details on how dpa values were calculated are described in the Methods section. Converting fluence to dpa allows the effects of the individual ions i n CdO to be normalized with respect to one another, as shown in Figure 1 b , in which transport property curves follow similar trends for all ions and irradiation energies explored here.

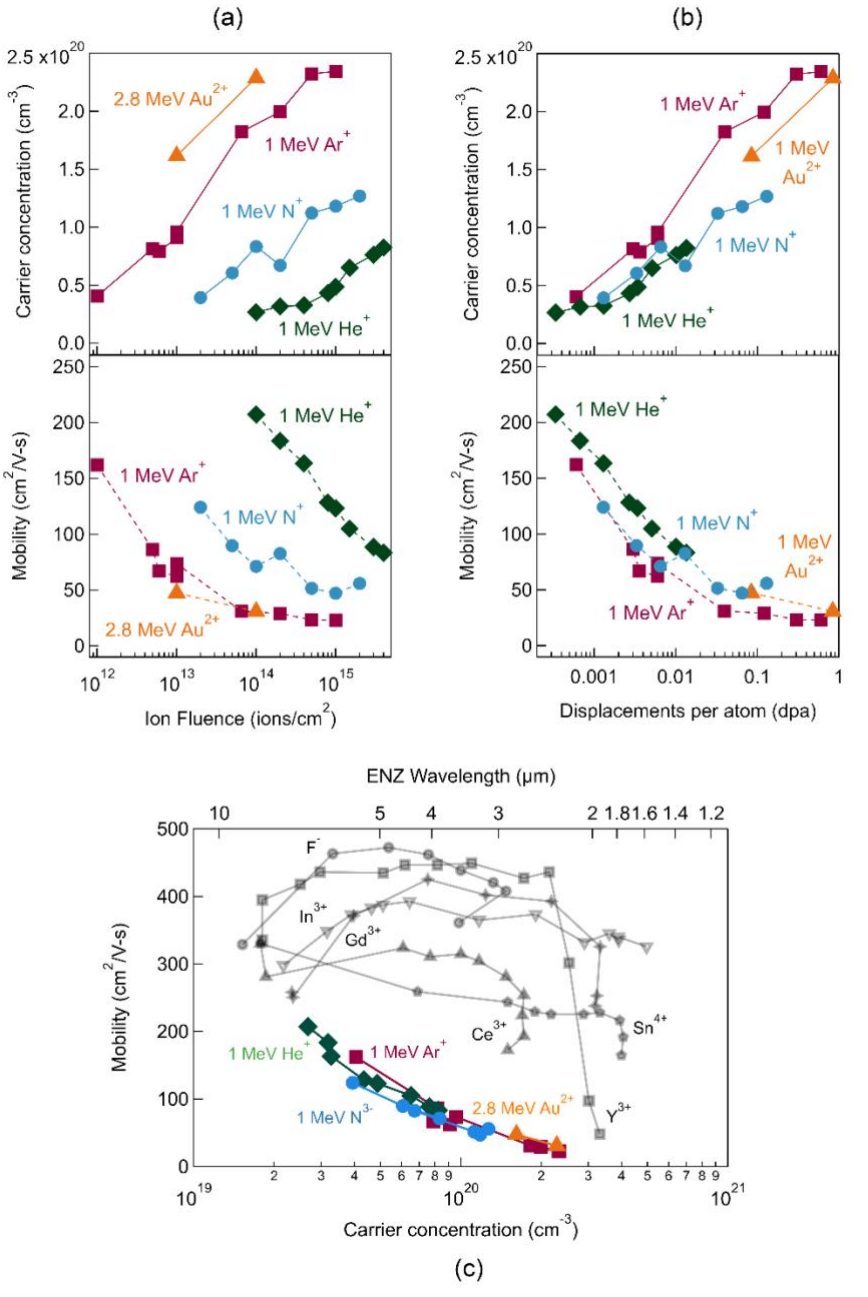


Figure 1 - Carrier concentration and mobility as a function of (a) ion fluence (ions/cm$^2$) and (b) displacements per atom (dpa) . (c) Carrier concentration vs. mobility for the same irradiated CdO samples (color) plotted against data for CdO films with various donor dopants incorporated (gray) .[6–8,34] Calculated ENZ wavelengths corresponding to carrier concentrations are plotted on the top axis.

The CdO carrier concentration range accessible through ion irradiation is comparable to what can be achieved by doping during deposition. This is illustrated in Figure 1 c with data points for irradiated films provided in color and doped films in gray. To provide context for optical

properties, the wavelength at which the ENZ condition is observed as a function of carrier concentration is also denoted. The ENZ wavelength is calculated using the Drude model equation for the CdO dielectric function as described by Equation 1:

$$\varepsilon(\omega) = \varepsilon_\infty - \frac{\omega_p^2}{\omega^2 - i\omega\Gamma} \quad (1)$$

where $\varepsilon_\infty$ is the high frequency permittivity (~5.3 for CdO)[9], $\omega_p$ is bulk plasma frequency ($\omega_p = \sqrt{ne^2/m^*\varepsilon_0}$), $\omega$ is the incident/operational frequency, and $\Gamma$ is the damping coefficient. Because of the dependence of the real part of the permittivity tensor on changes in $\omega_p$, which is directly related to carrier concentration ($n$), controlling the carrier density enables direct tuning of the dielectric response and by extension, the ENZ wavelength. This tuning ability is amplified in CdO due to its relatively low effective mass (m* ~ 0.21).[9]

While carrier density can be tuned broadly via ion irradiation, electron mobility is significantly lower (as low as 20 $cm^2$/V-s) in heavily irradiated films with respect to doped films (illustrated in Figure 1 c) as irradiation likely introduces significant additional scattering centers (i.e., the damage cascade) beyond those that are charged and contribute conduction band electrons. Conversely, substitutional defects created by doping during growth actually suppress native oxygen vacancy formation as a result of Le Chatelier's principle as observed in Dy-, Y-, F-, and In-doped CdO.[4,6–8] Oxygen vacancies are stronger scatterers than such substitutional defects due to their larger strain fields and double charge.[4,6,7] Electron mobility in CdO tends to follow the same trend as optical mobility in the mid-IR frequency range (see Supplemental Material Figure S4 ), which is inversely related to optical loss and is a strong indicator of plasmonic performance.[4,6,9,35] Although mobilities in irradiated films are lower than in doped materials, they still fall between 50-200 $cm^2$/V-s for much of the fluence range, which is still higher than that of many other semiconductor plasmonic materials within the same carrier density range.[36–40] Ultimately, irradiated CdO retains sufficiently low loss for supporting plasmonic resonances, and for many nanophotonic applications.

Ion irradiation can impact CdO crystallinity and microstructure, as irradiation-induced point defects are accompanied by strain within the CdO lattice, which is quantified here by x-ray diffraction (XRD). Although no additional phases form during the ion irradiation process (Figure

2 a), there is a clear expansion of the out-of-plane lattice constant indicated by the CdO <100> peaks shifting to lower 2θ values with increased damage (Figure 2 b). Note that $Al_2O_3$ (036) peaks are observed due to the *r*-plane sapphire substrate. However, despite the damage introduced, there is no significant impact to the surface morphology as shown by atomic force microscopy (AFM) data in Figure 2 c-f. The diagonal features in these micrographs show the history of the step-and-terrace morphology of the underlying substrate. Due to the epitaxial growth and smooth nature of the films, this morphology is apparent on the surface and remains present even after irradiation treatments. This lack of surface morphology change was observed for all ions explored, and the AFM micrographs in Figure 2 c-f represent Ar-irradiated CdO which encompassed the widest dpa range investigated for a single ion species in this study.

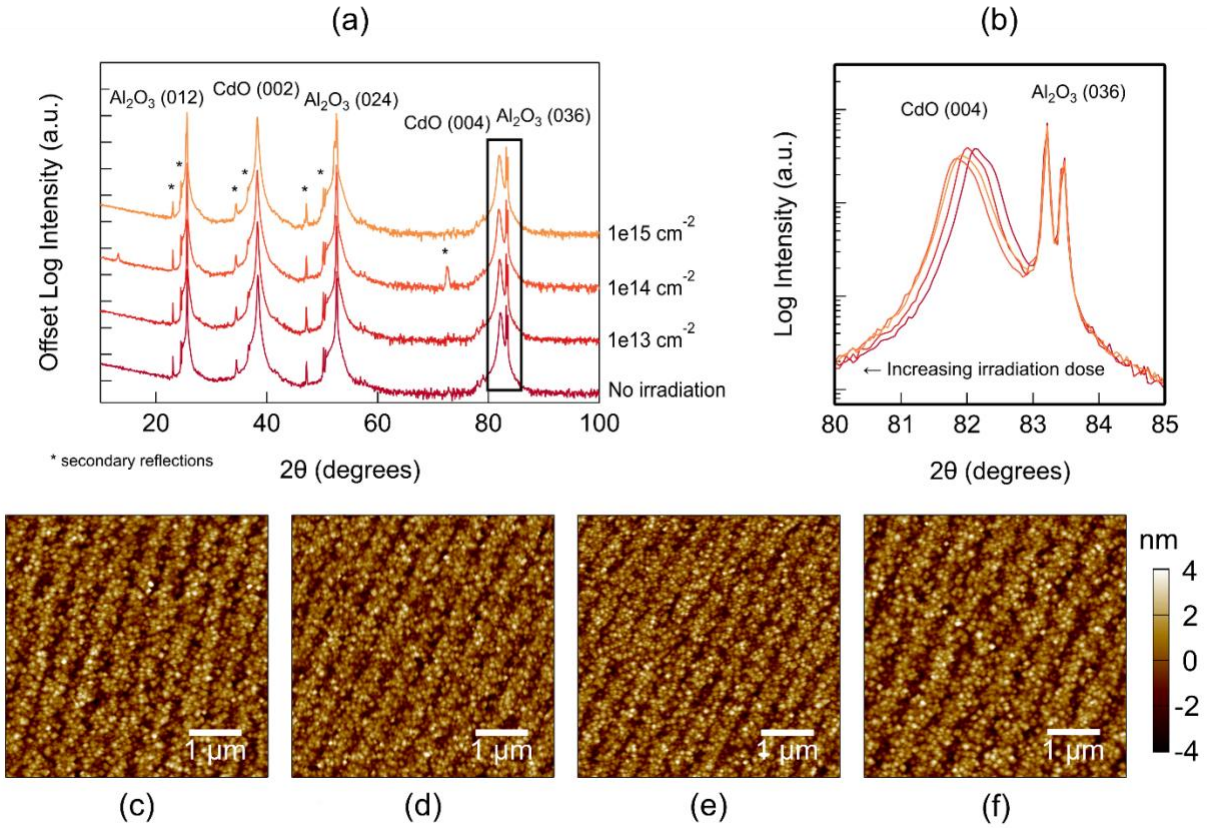


Figure 2 - (a) θ-2θ XRD scans for an untreated CdO film and films treated with 1 MeV $Ar^+$ ion irradiation at doses of $1\times10^{13}$ ions/cm$^2$, $1\times10^{14}$ ions/cm$^2$, and $1\times10^{15}$ ions/cm$^2$. The CdO peak shift is more closely highlighted in (b). Height retrace AFM micrographs for (c) a CdO thin film with no irradiation treatment and films treated with 1 MeV $Ar^+$ ions at (d) $1\times10^{13}$ ions/cm$^2$, (e) $1\times10^{14}$ ions/cm$^2$, and (f) $1\times10^{15}$ ions/cm$^2$.

The characterization results discussed thus far provided guidelines for fabricating laterally patterned CdO homostructures. 100-nm CdO films grown on 50 nm of Pt on *r*-plane $Al_2O_3$

substrates were patterned over 5×5 mm areas to exhibit flat gratings consisting of alternating high and low carrier concentration regions. This geometry was designed to support SPP propagation along the length of the gratings. To achieve such lateral patterning, films were exposed to 1 MeV $Ar^+$ ion irradiation at $1\times10^{13}$ ions/cm$^2$ fluence within the open regions of a 3- μm thick positive photoresist (SPR 955) patterned mask. This thickness was determined sufficient to effectively block ions by SRIM calculations (see Supplemental Material) based on the photoresist composition and density. $Ar^+$ was selected here as it consistently generated a high flux ion beam, enabling relatively short times to reach desired doses. After ion irradiation, samples were sonicated in toluene to remove the photoresist mask and were subsequently exposed to an oxygen plasma to etch away any remaining polymer residue. Additional fabrication details can be found in the Methods section.

Scattering-type scanning near-field optical microscopy (s-SNOM) measurements were performed to spatially map the infrared optical properties across the patterned regions. While measuring at an energy between the plasma frequencies (Re(ε)=0) of the two regions would yield maximum near-field contrast, limitations of available laser sources restricted measurements to laser frequencies below 2000 cm$^{-1}$ and thus below the plasma frequencies of both regions, as shown in Figure 3 a . The d ielectric functions presented here were extracted from ellipsometry measurements on control samples of non-irradiated and blanket ion irradiated CdO at an equivalent fluence as the patterned films ($1\times10^{13}$ ions/cm$^2$). Strong optical contrast between alternating regions is apparent, which is induced by the permittivity difference. Importantly, the optical signal within each region is uniform, implying high sample quality. Furthermore, the s-SNOM image indicates a relatively sharp (~400 nm) transition and uniform optical interfaces between the alternating regions. A SNOM line profile from which this transition length was determined is included in the Supplemental Material. This transition region occurs due to slight slopes in the mask walls (SEM image in Supplemental Material); however, this region is still relatively small compared to the grating widths (5 μm). Further, AFM topography data (Figure 3 c ) was collected simultaneously with s-SNOM optical measurements over the same patterned region confirming that the local optical property variations are not correlated to any morphological features.

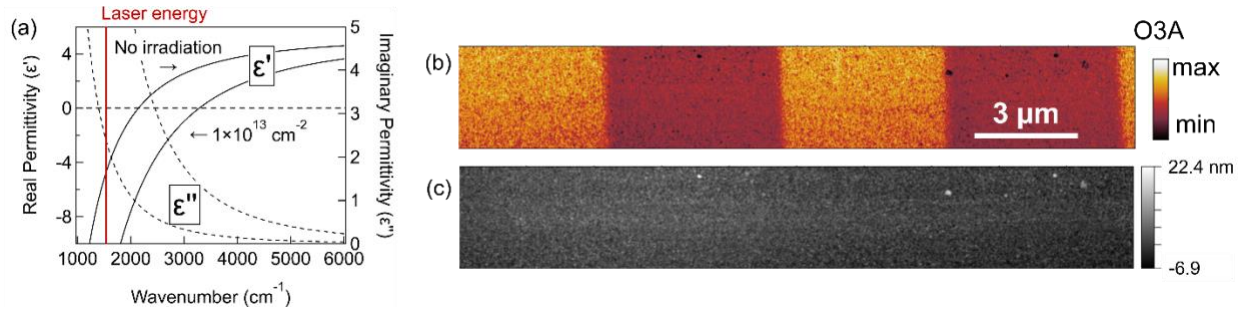


Figure 3 - (a) s-SNOM image of irradiation patterned CdO thin film collected as the third harmonic near-field optical amplitude (O3A) with (b) AFM image measured simultaneously. (c) Real permittivities of the non-irradiated and irradiated regions with dotted black line indicating the zero crossing point and the solid red line denoting the laser energy used for the s-SNOM measurements.

To characterize the overall optical response of the patterned lateral homostructure, far-field optical measurements were conducted using variable-angle reflectance spectroscopy. This data is used to generate reflectivity maps (shown in Figure 4 ), plotted as the ratio of p- to s-polarized light, where darker regions correspond to absorption features at a particular energy measured at a given incident angle. Such maps are analogous to dispersion maps ($\omega$ vs. $k$), as wavevector ($k$) is directly proportional to incident angle. Reflectivity maps for films irradiated at constant fluence (1 MeV $Ar^+$, $1\times10^{13}$ ions/cm$^{-2}$) with varying grating periodicity (6, 8, 10, 12 μm) are calculated by FEM in Figure 4 a-d, which correspond well to experimental data in Figure 4 e-h. For each reflectivity map, three distinct dispersive absorption features are observed, each of which shifts to higher incident angle (and therefore higher $k$) with increasing periodicity. Note that these modes occur only when the film is oriented with the grating lines parallel to the incident beam during measurement as illustrated in Supplemental Material Figure S10 ). Light incident parallel to the grating fins is able to acquire momentum $k_m$ in the orthogonal direction from the grating, leading to an excitation which propagates diagonally across the grating surface. In general, the dispersive nature here arises from SPP modes being supported by diffraction gratings. Such gratings enable SPP modes to be excited from free space despite occurring to the right of the light line due to auxiliary momentum supplied by the periodicity of the grating geometry.[5] The in-plane momentum of these modes is discussed in more depth through Equation 7 in the Methods section. This relationship also explains the shift to higher wavevector with increasing grating periodicity.

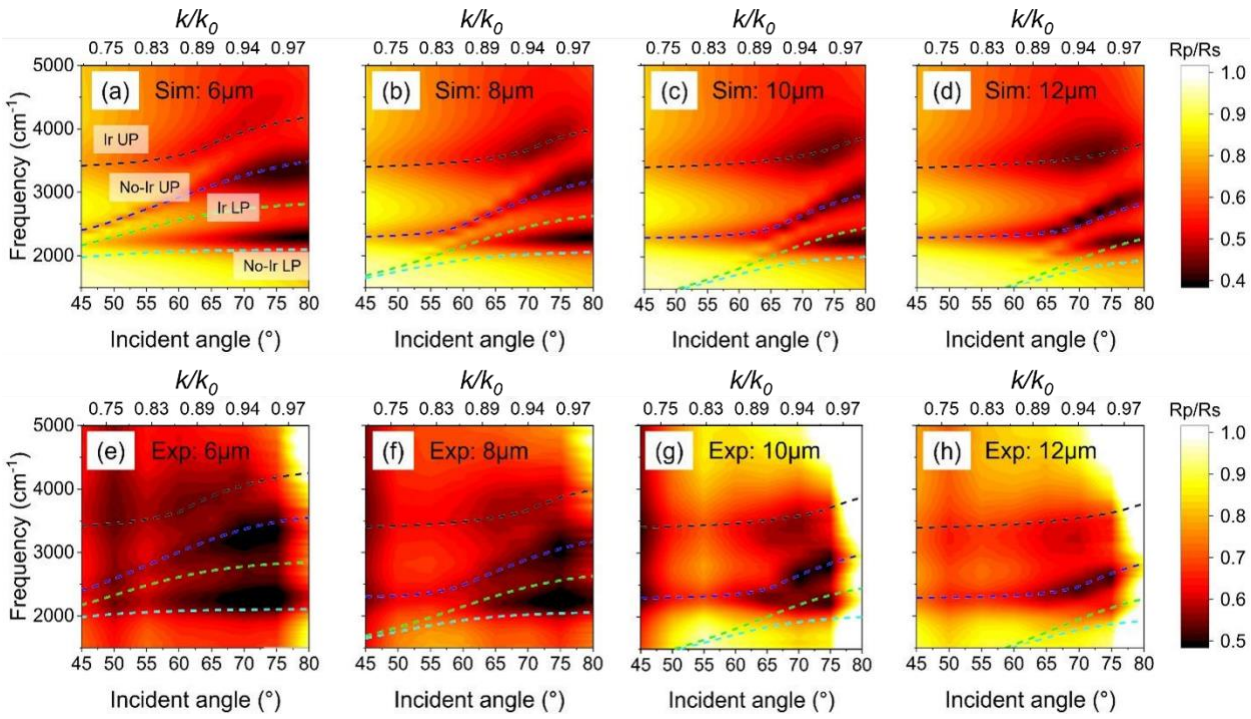


Figure 4 - Dispersion maps for (a-d) simulated and (e-h) experimental variable-angle reflectance spectroscopy data for in-plane patterned CdO lateral homostructures with varying periodicity (6, 8, 10, 12 μm). Dashed lines overlaying the dispersion maps are strong coupling simulation data for the upper and lower polaritons (UP and IP, respectively) of the irradiated and non-irradiated CdO modes (Ir and No-IR, respectively), assuming a CdO thickness of 100 nm.

The CdO grating on Pt system supports three bare modes, one from each CdO SPP (irradiated and non-irradiated regions) and a third from the extended SPP on the Pt substrate, which couples to both CdO modes. Although the frequency is low compared to the Pt plasma frequency, strong coupling is still achieved because the CdO layers are situated at the Pt surface where the SPP electric field intensity is large. The hallmarks of strong coupling can be observed by solving the analytical trilayer dispersion relation in each grating region as described in the Methods section. Although the emergence of strongly coupled branches is clear from analysis of the modal dispersion, it is not possible to form a Hopfield model[41] describing the coupled modes because the underlying bare modal dispersions cannot be accessed in the absence of strong coupling. The presence of the CdO film alters the SPP dispersion even in the absence of any longitudinal resonance.

We calculate the bare modes by calculating the modes of each trilayer grating fin in isolation. As we assume in each case that the Pt SPP is entirely confined in the trilayer studied, while in the full system one Pt SPP extends over the entire substrate that sees both CdO types, the number of modes

in the system is over-estimated by 1. Our model is however, free of tunable parameters and is able to reproduce both the spectral position and the slope of the polariton dispersion. The resulting zone-folded dispersions are overlaid onto the reflectivity maps in Figure 4 . Data for the trilayer containing irradiated CdO are shown by the black-dashed (upper polariton, UP) and green-dashed (lower polariton, LP) lines respectively, while that for non-irradiated CdO are shown by the blue-dashed (upper polariton, UP) and cyan-dashed (lower polariton, LP) lines, respectively. There is good agreement within the spectral window between the non-irradiated and irradiated CdO plasma frequencies, indicating the simulations provide a good approximation of the underlying interactions.

As this model assumes each CdO variety fills the plane, it over-estimates the coupling between the CdO layers and the Pt SPP. In the grating system the Pt SPP is distributed over the entire surface, while each CdO variety only occupies half the plane. This discrepancy leads to poor replication of the upper and lower polariton branches in Figure 4 . A better fit can be achieved by considering a 50 nm CdO film, as shown in Supplemental Figure S11 . This reduces the coupling rate by around 2, compensating for the over-estimation.

A summary of the samples discussed here is provided in Table I along with spectral positions and quality (Q)-factors of resonances. Q-factors are determined by fitting Lorentzian oscillators to experimental reflectance spectra at 70-degree incidence angle and defined by peak position ($cm^{-1}$) divided by full width at half maximum (FWHM). The Q-factor corresponds to the energy stored with respect to the damping rate. Additional fitting details are described in the Supplemental Material.

Table I - Summary of pattern irradiated samples with varying grating periodicity discussed in Figure 4 .

| Sample | Periodicity (μm) | Ion Fluence ($ions/cm^2$) | Center ($cm^{-1}$) | FWHM ($cm^{-1}$) | Q |
|---|---|---|---|---|---|
| 1 | 6 | $1\times10^{13}$ | 2255.4 | 603.23 | 3.7 |
| | | | 3254.8 | 1141.8 | 2.9 |
| | | | 4246.2 | 538.2 | 7.9 |
| 2 | 8 | $1\times10^{13}$ | 2210.7 | 544.8 | 4.1 |
| | | | 2842.4 | 728.1 | 3.9 |
| | | | 3816.3 | 1868.9 | 2.0 |

| | | | | | |
|---|---|---|---|---|---|
| 3 | 10 | $1\times10^{13}$ | 2151 | 413.8 | 5.2 |
| | | | 2586.9 | 560.9 | 4.6 |
| | | | 3499.1 | 2232.7 | 1.6 |
| 4 | 12 | $1\times10^{13}$ | 2003.5 | 424.1 | 4.7 |
| | | | 2395.0 | 456.5 | 5.2 |
| | | | 3246.9 | 2722.2 | 1.2 |

## Conclusions

This report demonstrates flat plasmonic lateral homostructures fabricated by 1 MeV $Ar^+$ ion irradiation on CdO thin films through a patterned photoresist mask. This process results in sharp optical interfaces between irradiated and non-irradiated regions, which are evident in scanning near-field optical microscopy measurements. We demonstrate patterned grating structures that support dispersive (SPP) resonances in both irradiated and non-irradiated regions, which exhibit strong coupling behavior with underlying Pt layers. This study also involved an analysis of transport, crystalline, and morphological properties as a function of irradiation fluence with $He^+$, $N^+$, $Ar^+$, and $Au^{2+}$ ions. Carrier concentration increases and mobility decreases with dose as native donor defects are formed from the irradiation and also act as charge scattering sites. Increased defect density from irradiation damage results in strain to the CdO lattice with little-to-no effect on surface morphology. This study serves as a basis for future work in engineering nanophotonic devices by modulating lateral variations in permittivity, such as controlling spatial coherence of thermal emission, local control of the dielectric permittivity for nanophotonic device design[42], and on-chip photonic devices.

## Methods

### *CdO Thin Film Growth*

CdO thin films were deposited on either *r*-plane (012) $Al_2O_3$ single crystal substrates (MSE Supplies, LLC) or 50 nm (111) oriented Pt grown on (100) Si single crystal substrates (supplied by YINCAE Advanced Materials, LLC). The sputtering process used high-power impulse magnetron sputtering (HiPIMS, Starfire Industries Impulse Pulsed Power Module and Advanced Energy MDX 1.5K DC power supply) from a 2-inch 99.9999% pure Cd metal target in a mixed argon (20 sccm) and oxygen (14.4 sccm) atmosphere. The magnetron was oriented in a sputter-down geometry at a 45-degree incidence angle. Substrates were adhered to a stainless-steel sample

holder using silver paint (Ted Pella). Depositions occur at 400°C with a total pressure of 14 mTorr. HiPIMS drive conditions are 800-Hz frequency and 80-µs pulse time, producing a 1250-µs period and 6.4% duty cycle.

*Displacement Damage Dose and Displacements per Atom Calculations*

Dpa can be modeled using the Stopping and Range of Ions in Matter (SRIM) software[43]. These calculations used the Ion Distribution and Quick Calculation of Damage mode and modeled a total of 40,000 ions. The target densities for the CdO film and $Al_2O_3$ substrate were 8.14 g/cm$^3$ and 3.95 g/cm$^3$, respectively, based on densities obtained from x-ray reflectivity fits. SRIM calculated displacement energies of 25 eV and 28 eV for Cd and O, respectively in the film.

Dpa is calculated using the equation:

$$dpa = \frac{v\phi t}{Nx} \quad (4)$$

Where $v$ is the total number of displacements , $\phi$ is the ion flux, $t$ is the irradiation time, $N$ is the number density of the CdO, and $x$ is depth. The average of the top 10 maximum values of dpa as a function of depth (*dpa(D)*) is used as the singular value of dpa for a given fluence. Further details about using SRIM to calculate dpa is discussed in Ref. [44].

*Photoresist patterning and removal*

Laterally patterned CdO films were masked using a positive photoresist (SPR 955) patterned into a grating structure. Before depositing the photoresist, a 100 nm layer of poly(methyl methacrylate) (PMMA) was spin coated onto the CdO surface followed by a 3 minute bake at 180°C to polymerize the material. Here, PMMA acts as a protective barrier during the photoresist develop process which involved a rinse in deionized (DI) water which would interact with and etch CdO. Next, a 100 nm layer of polydimethylglutarimide (PMGI) was deposited on the PMMA layer, also followed by a 3-minute bake at 180°C. PMGI was used as an intermediary layer to prevent intermixing that could occur between the PMMA and SPR 955 layers. It is also a more heat resistant polymer intended to protect the PMMA from hardening due to local heating which may

occur during ion irradiation and make it difficult to remove residual polymer after irradiation treatments. Finally, a 3 μm thick layer of SPR 955 photoresist was deposited followed by a 2-minute bake at 105°C. The grating was patterned by an ultraviolet (UV) direct write process, then the SPR 955 was developed in CD-26 followed by a DI water rinse, and then dried. To remove the PMMA and PMGI remaining in the grating openings, the sample was treated with a deep UV flood which was blocked by the SPR 955 in the grating regions. 101A developer was used to remove the PMGI and the remaining PMMA was removed by a toluene rinse.

After ion irradiation on patterned CdO films, polymer and photoresist were removed first by a heated sonication (40°C) in an acetone bath for 3 hours, followed by a toluene bath for 24 hours. After this process, about 10 nm of polymer remained, which was removed by an oxygen plasma etch, leaving behind a smooth CdO surface. A schematic of the photolithography process, irradiation treatment, and final patterned material is illustrated in Figure 5a-f. SEM images in the Supplemental Material show top-down views of the patterned samples before and after mask removal. The sidewalls of the resist are not perfectly straight, with bleeding edges of about 400-500 nm based on ImageJ analysis. However, line profiles of SNOM measurements (also in Supplemental Material) suggest a transition region width of about 400 nm. Despite this transition region, the SNOM image in Figure 4 shows sharp optical contrast between neighboring regions. Further, experimental dispersion maps align exceptionally well with calculations, though slight deviations may be attributed to these blurred edges. While the direct write method was used to pattern samples for proof-of-concept experiments demonstrated here, future studies may consist of hard masking or electron beam lithography for more precise patterning.

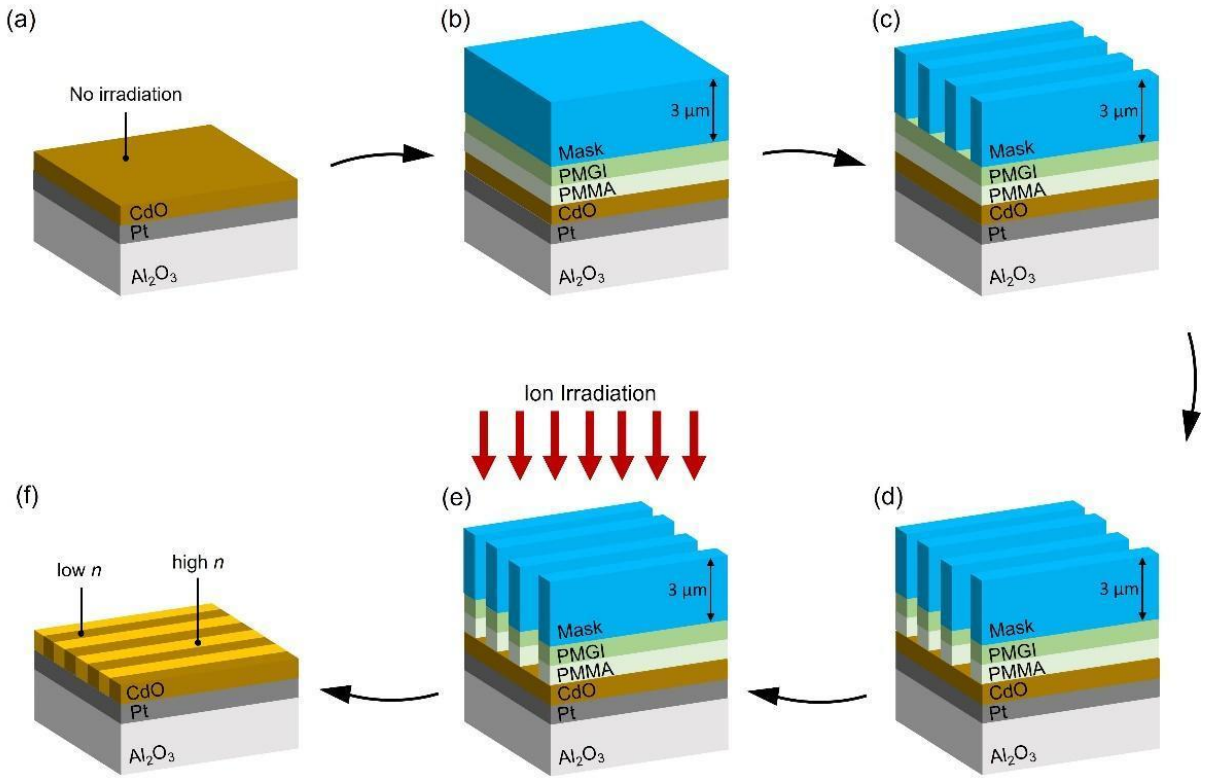


Figure 5 - Illustration of irradiation patterning process. (a) UID CdO film grown on a layer of Pt on a Si substrate. (b) Layers of polymer and photoresist blanket deposited on UID CdO. (c) Layered structure with photoresist mask developed to form grating pattern. (d) Layered structure after developing polymer layers to expose underlying CdO. (e) Ion irradiation treatment on a CdO film through patterned mask. (f) Permittivity patterned CdO after mask removal.

*Ion Irradiation*

The RDI Dynamitron at the University at Albany Ion Beam Laboratory was used to irradiate CdO thin films at nominally room temperature at a 6-degree angle to avoid channeling, with several different ions at 1 MeV energies: 1 MeV $He^+$ ($1\times10^{14}$ - $1\times10^{15}$ ions/cm$^2$), 1 MeV $N^+$ ($2\times10^{13}$ - $2\times10^{15}$ ions/cm$^2$), and 1 MeV $Ar^+$ ($1\times10^{12}$ - $1\times10^{15}$ ions/cm$^2$). The HVE 6 MV Tandem at Sandia National Laboratories was used to irradiate CdO films with 2.8 MeV $Au^{2+}$ ions at fluences of $1\times10^{13}$ - $1\times10^{14}$ ions/cm$^2$ at nominally room temperature and direct normal incidence.

*Near-field measurement*

Near-field nano-imaging experiments were carried out in a commercial Neaspec (www.neaspec.com) s-SNOM and nano-FTIR based around a tapping-mode atomic force microscope. A metal-coated Si-tip of apex radius R ≈ 20 nm that oscillates at a frequency of Ω ≈

280 kHz and tapping amplitude of about 100 nm is illuminated by a laser beam at an angle 60° off normal to the sample surface. Background signals are efficiently suppressed by demodulating the detector signal at harmonics of the tip oscillation frequency and employing pseudo-heterodyne interferometric detection.

*Far-field optical characterization*

Reflectance measurements were performed using an IR variable-angle spectroscopic ellipsometer (IR-VASE). Because the patterned region (5×5 mm square) was smaller than the IR beam spot size (~10 mm diameter), Kim wipes were used to cover the film surrounding this area to prevent additional reflections. To maintain consistent reflection intensity, this Kim wipe window mask was also used for collecting background data on platinum films and for measuring witness samples. Measurements were conducted between 45–80-degree incidence angles (defined as angle from surface normal), with background measurements at each angle subtracted from film measurements.

*Numerical simulations of far-field response*

FEM simulations were performed in CST studio suite 2019 to simulate the far-field response of the sub-diffraction gratings. The unit cell boundary conditions used in the simulations assume infinite periodicity of the gratings. Unit cell size is the same as in experiments. Standard transverse electric (TE) and transverse magnetic (TM) modes are used as excitation sources and reflections are collected.

*Strong coupling simulations*

We calculate the dispersion in each Vacuum / CdO / Pt trilayer analytically, using the standard result[45]

$$exp\,[-4\,k_1 a] \;=\; \frac{k_1/\epsilon_1 + k_2/\epsilon_2}{k_1/\epsilon_1 - k_2/\epsilon_2}\frac{k_1/\epsilon_1 + k_3/\epsilon_3}{k_1/\epsilon_1 - k_3/\epsilon_3} \qquad (5)$$

where $k_1$ ($\epsilon_1$) is the out-of-plane wavevector (dielectric function) in the CdO layer, $k_2$ ($\epsilon_2$) is the out-of-plane wavevector (dielectric function) in the vacuum superstrate, $k_3$ ($\epsilon_3$) is the out-of-plane wavevector (dielectric function) in the Pt substrate and $a$ is the CdO layer thickness. The out-of-plane wavevector relates to the in-plane wavevector $k_{\parallel}$ through

$$k_i = \sqrt{{k_\parallel}^2 - {k_0}^2 \epsilon_i}\,, \tag{6}$$

where $k_0 = \omega/c$ is the free-space wavevector.

The roots of this relation are the dispersion of the trilayer excitations on an unpatterned substrate. In a grating these modes are folded by the periodicity, making guided excitations accessible within the lightline according to

$$k_\parallel = |k_0[sin\,\theta\,cos\,\phi, sin\,\theta\;\; sin\,\phi] + [\frac{2\,\pi\,m}{\Lambda_x}, \frac{2\,\pi\,n}{\Lambda_y}]\,|, \tag{7}$$

where $\theta$ ($\phi$) are the azimuthal (axial) angle of the incident excitation, $\Lambda_x$ ($\Lambda_y$) are the periodicity of the grating along the $x$ ($y$) axis, and $m, n$ are integers representing the diffraction order. Note that in the experiment under study $\Lambda_y = \infty$ and $\phi = 90°$.

*Transport measurements*

Carrier concentration and electron mobility were quantified by Hall effect measurements in the van der Pauw configuration using an Ecopia HMS-3000 with a 0.545 T magnet. Samples were etched with 5% hydrochloric acid into 5 × 5 mm squares using semiconductor dicing tape masks to achieve appropriate van der Pauw geometry and improve accuracy of the measurements.

*Film Quality Characterization*

Film thickness and crystallinity are characterized via a PANalytical Empyrean x-ray diffractometer in a parallel beam geometry with a double-bounce monochromator and a parallel-plate collimator. X-ray reflectivity (XRR) $\omega - 2\theta$ scans just above the angle of total external reflection is used to assess film thickness. Symmetric $2\theta - \omega$ x-ray diffraction (XRD) scans are used to assess crystal quality. Out-of-plane mosaicity is characterized by $\omega$ rocking curve scans about the CdO (200) peak. Surface morphology of films is characterized by atomic force microscopy (AFM) collected by an Asylum MFP-3D AFM in tapping mode.

**Acknowledgements**

A.J.C., M.J.T., J.-P.M., and J.D.C. gratefully acknowledge support for this work by Office of Naval Research Grant N00014-22-12035. J.D.C., J.-P.M, and M.H. acknowledge support from the Army Research Office Research Grant W911NF-21-1-0119. Irradiation experiments were performed at the Ion Beam Laboratory at the University at Albany with help from Kevin Wynne, Daniele Cherniak, Chris Righi, and Andrew Knutson, and at the Center for Integrated Nanotechnology (CINT) at Sandia National Laboratory by Khalid Hattar and Eric Lang. Lithography was performed by Michael Labella at the Pennsylvania State University Nanofabrication Lab within the Materials Research Institute. S.D.L. gratefully acknowledges support from the Leverhulme Trust Grant No. RPG-2022-037. This work was performed, in part, at the Center for Integrated Nanotechnologies, an Office of Science User Facility operated for the U.S. Department of Energy (DOE) Office of Science. Sandia National Laboratories is a multimission laboratory managed and operated by National Technology & Engineering Solutions of Sandia, LLC, a wholly owned subsidiary of Honeywell International, Inc., for the U.S. DOE's National Nuclear Security Administration under contract DE-NA-0003525. The views expressed in the article do not necessarily represent the views of the U.S. DOE or the United States Government.

**References**

1. Naik, G. V., Shalaev, V. M. & Boltasseva, A. Alternative plasmonic materials: Beyond gold and silver. *Adv. Mater.* **25**, 3264–3294 (2013).

2. Zhong, Y., Malagari, S. D., Hamilton, T. & Wasserman, D. M. Review of mid-infrared plasmonic materials. *J. Nanophotonics* **9**, 093791 (2015).

3. Babicheva, V. E., Boltasseva, A. & Lavrinenko, A. V. Transparent conducting oxides for electro-optical plasmonic modulators. *Nanophotonics* **4**, 165–185 (2015).

4. Sachet, E. *et al.* Dysprosium-doped cadmium oxide as a gateway material for mid-infrared plasmonics. *Nat. Mater.* **14**, 414–420 (2015).

5. Folland, T. G., Nordin, L., Wasserman, D. & Caldwell, J. D. Probing polaritons in the mid- to far-infrared. *J. Appl. Phys.* **125**, 191102 (2019).

6. Cleri, A. *et al.* Mid-wave to near-IR optoelectronic properties and epsilon-near-zero behavior in indium-doped cadmium oxide. *Phys. Rev. Mater.* **5**, 035202 (2021).

7. Kelley, K. P., Sachet, E., Shelton, C. T. & Maria, J.-P. High mobility yttrium doped cadmium oxide thin films. *APL Mater.* **5**, 076105 (2017).

8. Runnerstrom, E. L., Kelley, K. P., Sachet, E., Shelton, C. T. & Maria, J.-P. Epsilon-near-zero modes and surface plasmon resonance in fluorine-doped cadmium oxide thin films. *ACS Photonics* **4**, 1885–1892 (2017).

9. Nolen, J. R. *et al.* Ultraviolet to far-infrared dielectric function of n -doped cadmium oxide thin films. *Phys. Rev. Mater.* **4**, 025202 (2020).

10. Campione, S., Brener, I. & Marquier, F. Theory of epsilon-near-zero modes in ultrathin films. *Phys. Rev. B* **91**, 121408 (2015).

11. Vassant, S., Hugonin, J.-P., Marquier, F. & Greffet, J.-J. Berreman mode and epsilon near zero mode. *Opt. Express* **20**, 23971 (2012).

12. Cleri, A. J. *et al.* Tunable, homoepitaxial hyperbolic metamaterials enabled by high mobility CdO. *Adv. Opt. Mater.* **11**, 2202137 (2023).

13. Kelley, K. P. *et al.* Multiple epsilon-near-zero resonances in multilayered cadmium oxide: Designing metamaterial-like optical properties in monolithic materials. *ACS Photonics* **6**, 1139–1145 (2019).

14. Runnerstrom, E. L. *et al.* Polaritonic hybrid-epsilon-near-zero modes: Beating the plasmonic confinement vs propagation-length trade-off with doped cadmium oxide bilayers. *Nano Lett.* **19**, 948–957 (2019).

15. Lu, G. *et al.* Engineering the spectral and spatial dispersion of thermal emission via polariton–phonon strong coupling. *Nano Lett.* **21**, 1831–1838 (2021).

16. Lu, G., Tadjer, M., Caldwell, J. D. & Folland, T. G. Multi-frequency coherent emission from superstructure thermal emitters. *Appl. Phys. Lett.* **118**, 141102 (2021).

17. Lu, G. *et al.* Narrowband polaritonic thermal emitters driven by waste heat. *ACS Omega* **5**, 10900–10908 (2020).

18. Greffet, J.-J. *et al.* Coherent emission of light by thermal sources. *Nature* **416**, 61–64 (2002).

19. Khurgin, J. B. How to deal with the loss in plasmonics and metamaterials. *Nat. Nanotechnol.* **10**, 2–6 (2015).

20. Boltasseva, A. & Atwater, H. A. Low-Loss Plasmonic Metamaterials. *Science* **331**, 290–291 (2011).

21. Khurgin, J. B. & Boltasseva, A. Reflecting upon the losses in plasmonics and metamaterials. *MRS Bull.* **37**, 768–779 (2012).

22. Fang, Y. & Sun, M. Nanoplasmonic waveguides: towards applications in integrated nanophotonic circuits. *Light Sci. Appl.* **4**, e294–e294 (2015).

23. Shirmanesh, G. K., Sokhoyan, R., Wu, P. C. & Atwater, H. A. Electro-optically tunable multifunctional metasurfaces. *ACS Nano* **14**, 6912–6920 (2020).

24. Rosenberg, A. *et al.* Flat mid-infrared composite plasmonic materials using lateral doping-patterned semiconductors. *J. Opt.* **16**, 094012 (2014).

25. Salman, J. *et al.* Flat optical and plasmonic devices using area-selective ion-beam doping of silicon. *Adv. Opt. Mater.* **6**, 1701027 (2018).

26. Mei, H. *et al.* Tuning carrier density and phase transitions in oxide semiconductors using focused ion beams. *Nanophotonics* **11**, 3923–3932 (2022).

27. Sarkar, A. *et al.* Depth resolved defect characterization of energetic ion irradiated ZnO by positron annihilation techniques and photoluminescence. *J. Phys. Condens. Matter* **32**, 085703 (2020).

28. Pal, S. *et al.* Clustered vacancies in ZnO: chemical aspects and consequences on physical properties. *J. Phys. Appl. Phys.* **51**, 105107 (2018).

29. Speaks, D. T. *et al.* Fermi level stabilization energy in cadmium oxide. *J. Appl. Phys.* **107**, 113706 (2010).

30. King, P. D. C. *et al.* Unification of the electrical behavior of defects, impurities, and surface states in semiconductors: Virtual gap states in CdO. *Phys. Rev. B* **79**, 035203 (2009).

31. Messenger, S. R. *et al.* Nonionizing energy loss (NIEL) for heavy ions. *IEEE Trans. Nucl. Sci.* **46**, 1595–1602 (1999).

32. Messenger, S. R., Summers, G. P., Burke, E. A., Walters, R. J. & Xapsos, M. A. Modeling solar cell degradation in space: A comparison of the NRL displacement damage dose and the JPL equivalent fluence approaches†. *Prog. Photovolt. Res. Appl.* **9**, 103–121 (2001).

33. Norgett, M. J., Robinson, M. T. & Torrens, I. M. A proposed method of calculating displacement dose rates. *Nucl. Eng. Des.* **33**, 50–54 (1975).

34. Kelley, K. P. Mid-infrared plasmonics in cadmium oxide thin films. (North Carolina State University, 2018).

35. Lounis, S. D., Runnerstrom, E. L., Llordés, A. & Milliron, D. J. Defect chemistry and plasmon physics of colloidal metal oxide nanocrystals. *J. Phys. Chem. Lett.* **5**, 1564–1574 (2014).

36. Brewer, S. H. & Franzen, S. Optical properties of indium tin oxide and fluorine-doped tin oxide surfaces: correlation of reflectivity, skin depth, and plasmon frequency with conductivity. *J. Alloys Compd.* **338**, 73–79 (2002).

37. Preissler, N., Bierwagen, O., Ramu, A. T. & Speck, J. S. Electrical transport, electrothermal transport, and effective electron mass in single-crystalline $In_2O_3$ films. *Phys. Rev. B* **88**, 085305 (2013).

38. Kirste, R. *et al.* Ge doped GaN with controllable high carrier concentration for plasmonic applications. *Appl. Phys. Lett.* **103**, 242107 (2013).

39. Akin, N., Kinaci, B., Ozen, Y. & Ozcelik, S. Influence of RF power on the opto-electrical and structural properties of gallium-doped zinc oxide thin films. *J. Mater. Sci. Mater. Electron.* **28**, 7376–7384 (2017).

40. Agashe, C. *et al.* Efforts to improve carrier mobility in radio frequency sputtered aluminum doped zinc oxide films. *J. Appl. Phys.* **95**, 1911–1917 (2004).

41. Hopfield, J. J. Theory of the Contribution of Excitons to the Complex Dielectric Constant of Crystals. *Phys. Rev.* **112**, 1555–1567 (1958).

42. Folland, T. G. *et al.* Reconfigurable infrared hyperbolic metasurfaces using phase change materials. *Nat. Commun.* **9**, 4371 (2018).

43. J. F. Ziegler, J. P. B. and U. L. *The Stopping and Range of Ions in Solids*. (Pergamon Press, New York, 1985).

44. Stoller, R. E. *et al.* On the use of SRIM for computing radiation damage exposure. *Nucl. Instrum. Methods Phys. Res. Sect. B Beam Interact. Mater. At.* **310**, 75–80 (2013).

45. Maier, S. A. *Plasmonics: Fundamentals and Applications*. (Springer US, New York, NY, 2007). doi:10.1007/0-387-37825-1.